Distributed Maximum Power Point Tracking of Photovoltaic Arrays: Novel Approach and System Analysis

Nicola Femia, *Member, IEEE*, Gianpaolo Lisi, Giovanni Petrone, Giovanni Spagnuolo, *Member, IEEE*, and Massimo Vitelli

***Abstract*—One of the major drawbacks of photovoltaic (PV) systems is represented by the effect of module mismatching and of partial shading of the PV field. Distributed maximum power point tracking (DMPPT) is a very promising technique that allows the increase of efficiency and reliability of such systems. Modeling and designing a PV system with DMPPT is remarkably more complex than implementing a standard MPPT technique. In this paper, a DMPPT system for PV arrays is proposed and analyzed. A dc and small-signal ac model is derived to analyze steady-state behavior, as well as dynamics and stability, of the whole system. Finally, simulation results are reported and discussed.**

***Index Terms*—Distributed generation, maximum power point tracking (MPPT) techniques, photovoltaic (PV) systems.**

I. Introduction

THE INCREASING concern over environmental issues and the advantages that photovoltaic (PV) energy generation offers, if compared to other renewable energy sources, particularly in terms of reliability, maintenance, and integrability, drew, in the last decade, great interest and remarkable investments in PV technology [1], [2].

A PV field is composed of a number of series-connected modules (strings) arranged in parallel. Usually, cells in a PV field are assumed to be of the same type, or even equal, but such a hypothesis is no longer valid if manufacturing tolerances and aging-related parametric drift are accounted for. Moreover, due to possible different orientations of modules and to shadowing effects, the PV field very often works in mismatching conditions, and the probability that some cells in a module or some modules in a string are potentially able to deliver strongly different currents is very high [3], [4]. To prevent one shadowed cell from narrowing the current path in a string, thus downgrading the other ones in the series and reducing the power production of the whole string, bypass diodes are usually placed in antiparallel to small groups of series-connected cells. In case of mismatching, this measure increases the power production of the PV field but makes its power versus voltage characteristic multimodal [4]. The presence of more than one peak in such a characteristic makes much more complicated the detection of the absolute maximum power point (MPP) of the PV field. Operation in any other point of the characteristic, due to fault of the MPP tracking (MPPT) technique in presence of mismatching conditions, causes a consistent drop in the overall system's efficiency [4]. In order to overcome such a drawback, a switching converter dedicated to each module [module integrated converter (MIC)] and performing the MPPT operation can be used [5]–[7]. Hereafter, a system composed of a PV module with a dedicated dc–dc converter will be referred to as self-controlled PV module (SCPVM). Although the acronym DMPPT does not appear in [5]–[7], in all these papers, the problem of DMPPT of PV systems is addressed. In particular, in [5], several dc–dc MIC topologies that are to be adopted in PV applications are considered, and a useful efficiency comparison among buck, boost, Cuk, and buck–boost is presented, but no dc or ac analysis is derived either for a single SCPVM or for a string of SCPVMs. In [6], an SCPVM is referred to as intelligent PV module. A prototype is presented and experimentally tested, but again, no dc or ac model is presented. In [7], the solution to the output power drop due to mismatching operating conditions among PV modules is again addressed via a DMPPT approach. In this case a parallel rather than a series connection of SCPVMs is considered. A dc–ac model is derived for a single SCPVM but not for a string of SCPVMs. It is worth noting that an accurate dc and ac analysis capable of describing steady-state operation, dynamic behavior and stability of a whole array of SCPVMs has not been presented so far in literature. The aim of this paper is to derive a dc and small-signal ac model of an array constituted by a given number of SCPVMs and to adopt it to study the impact of system parameters on effectiveness and stability of the proposed DMPPT technique.

Grid-connected inverters' input voltage usually ranges from 180 to 500 V. Therefore, a number of PV modules is usually connected in series to supply the inverter with an input voltage within its operating range, and identical strings are then connected in parallel to achieve the desired output power. For these reasons, a system composed by parallel strings of a number of

Manuscript received October 8, 2007; revised March 31, 2008.

N. Femia, G. Petrone, and G. Spagnuolo are with the Department of Information and Electrical Engineering, University of Salerno, 84084 Fisciano, Italy (e-mail: gspagnuolo@unisa.it).

G. Lisi was with the Department of Information and Electrical Engineering, University of Salerno, 84084 Fisciano, Italy. He is now with National Semiconductor Corporation, Santa Clara, CA 95051 USA (e-mail: gianpaolo.lisi@nsc.com).

M. Vitelli is with the Department of Information Engineering, Second University of Naples, 81031 Aversa, Italy (e-mail: vitelli@unina.it).

Color versions of one or more of the figures in this paper are available online at http://ieeexplore.ieee.org.

Digital Object Identifier 10.1109/TIE.2008.924035

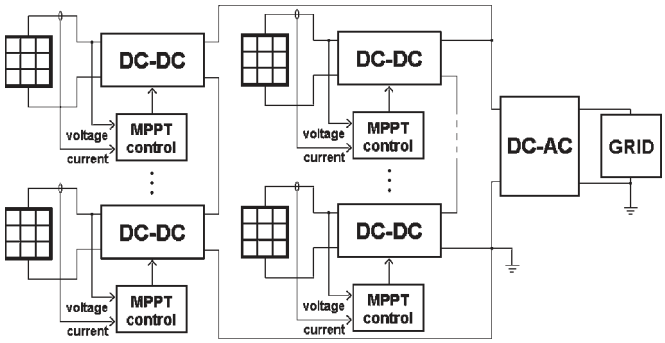

Fig. 1. Grid-connected PV system with distributed MPPT.

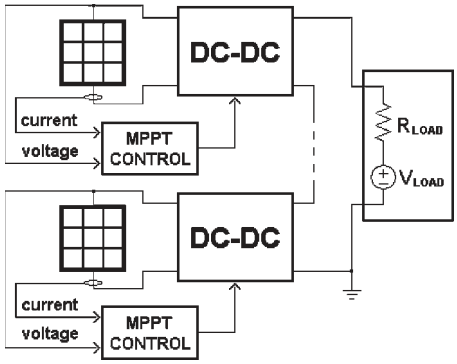

Fig. 2. Simplified model of a string of SCPVMs.

SCPVMs connected in series will be considered in this paper (Fig. 1). As a first-order approximation, it is possible to model the dc–ac conversion stage as a voltage source $V_{\rm LOAD}$ with a series resistance $R_{\rm LOAD}$; indeed, a PV inverter is capable of sinking whatever current in a certain range while keeping its input voltage regulated to a fixed average value [8].

This assumption greatly simplifies system's analysis because, as long as the value of $R_{\rm LOAD}$ is small compared to the output impedance of a string of SCPVMs, each string forms an independent loop with the equivalent model of the dc–ac conversion stage, and the analysis of the circuit of Fig. 1 can be simplified by resorting to the analysis of a single string of N SCPVMs (Fig. 2).

II. DC Analysis of a String of SCPVMs

For the system in Fig. 2, it is

$$P_{\rm tot} = \sum_{i=1}^{N} P_{{\rm pan}\,i} = \sum_{i=1}^{N} V_{{\rm pan}\,i} \cdot I_{{\rm pan}\,i} = \sum_{i=1}^{N} V_{{\rm pan}\,i} \cdot f_i(V_{{\rm pan}\,i}) \tag{1}$$

where $P_{\rm tot}$ is the total output power of the system, $P_{{\rm pan}\,i}$ is the output power of the ith PV module, and $I_{{\rm pan}\,i} = f_i(V_{{\rm pan}\,i})$ is its characteristic equation.

It is worth noting that, in presence of mismatching, even by adopting SCPVMs, it is not always possible to achieve the MPP of the overall system by simply tracking the MPP of each PV module. In principle, only step-up–down converters with unitary efficiency would be able to allow it. This aspect has not been sufficiently stressed in literature, except in a few papers (e.g., [5]). The effect of a limited conversion ratio due to the adopted dc–dc converter topology and of its efficiency will be discussed in this section. In particular, a dc model for a string of SCPVMs operating under mismatched irradiance will be derived. Other sources of mismatching among solar panels can be taken into account in a similar way.

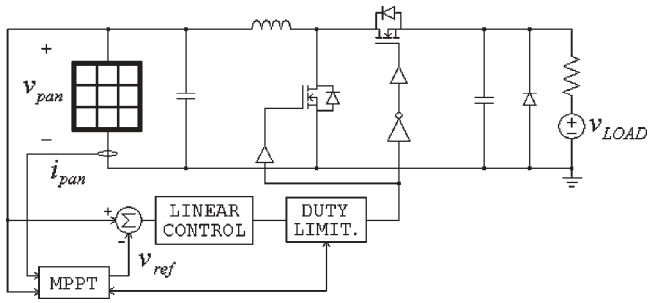

Fig. 3. Simplified schematic of an SCPVM employing a boost converter with synchronous rectification, input-voltage feedback control, and dynamic duty-cycle limitation.

The choice of the particular dc–dc converter topology that best suits a given application depends on the number of SCPVMs that each string is made of and on the $V_{\rm LOAD}$ value (see Fig. 2). In [5] and [9], the buck, boost, Cuk, and buck–boost topologies are considered as possible dc–dc PV module converters. Advantages and drawbacks of such topologies are examined in detail, and the conclusion is that, while flexible in voltage ranges, buck–boost and Cuk topologies are characterized by lower efficiencies and higher costs because of enhanced component stresses [10] and that the most promising solution for series-connected module integrated dc–dc converters in practical applications is generally represented by the boost converter. In this paper, a boost topology with synchronous rectification will be considered.

The MPPT of an SCPVM can be achieved by means of several standard MPPT techniques. A wide variety of them have been proposed in the literature, some of the most recent being described in [11]–[19]. In this paper, the perturb and observe (P&O) technique is considered due to its high performance and simple and cost-effective implementation [20]. In a system like that one shown in Fig. 1, every disturbance introduced on the output voltage, by the inverter and/or by other SCPVMs, directly propagates on the PV modules' output voltage. This may lead to instability or dynamic-performance degradation [8]. In this paper, a boost converter with linear input-voltage feedback control is considered (Fig. 3). In such a system, the P&O control variable is the reference voltage $V_{\rm ref}$. If the control loop is fast enough, disturbances in the output loop of the system do not significantly affect the operation of a single SCPVM [8]. The implementation of a dynamic duty-cycle limitation prevents output overvoltages when deep mismatching conditions occur. This aspect will be clarified later on. For simplicity of computation and ease of graphical representation of results, a string made of H SCPVMs operating under irradiance level SH and of L SCPVMs operating under irradiance level SL will be considered in the following (Fig. 4). Of course, it is $N = H + L$. It will be assumed that all the L SCPVMs are identical and that their MPPT controllers are synchronized. This assumption simplifies system analysis and simulation. Simulations including random delay between MPPT controllers

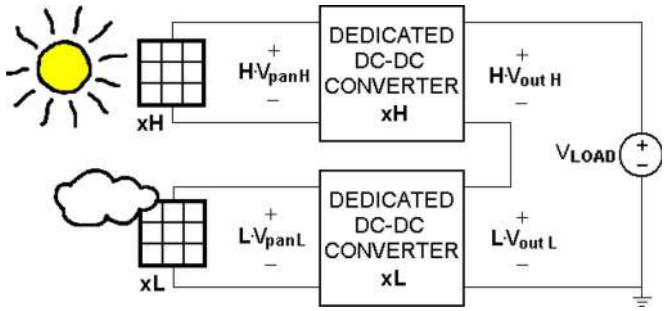

Fig. 4. Simplified model of a string of SCPVMs under uneven irradiation.

were also run and a negligible difference was found between these two approaches. The same assumption is also valid for the H SCPVMs.

The dc behavior of the system shown in Fig. 4 is described by

$$HV_{\text{out}\,H} + LV_{\text{out}\,L} = V_{\text{LOAD}} \tag{2}$$

$$I_{\text{out}\,H} = I_{\text{out}\,L} \tag{3}$$

$$V_{\text{out}\,H} = M(D_H)V_{\text{pan}\,H} \tag{4}$$

$$V_{\text{out}\,L} = M(D_L)V_{\text{pan}\,L} \tag{5}$$

$$I_{\text{out}\,H} = \frac{I_{\text{pan}\,H}}{M(D_H)} \tag{6}$$

$$I_{\text{out}\,L} = \frac{I_{\text{pan}\,L}}{M(D_L)} \tag{7}$$

$$I_{\text{pan}\,H} = f_H(V_{\text{pan}\,H}) \tag{8}$$

$$I_{\text{pan}\,L} = f_L(V_{\text{pan}\,L}). \tag{9}$$

Symbols used in (2)–(9) have the following meaning: $H(L)$, number of modules with irradiation $SH(SL)$; $V_{\text{out}\,H}(V_{\text{out}\,L})$, output voltage of an SCPVM with irradiation $SH(SL)$; $I_{\text{out}\,H}(I_{\text{out}\,L})$, output current of an SCPVM with irradiation $SH(SL)$; $D_H(D_L)$, duty cycle of an SCPVM with irradiation $SH(SL)$; $M(D)$, conversion ratio of the dc–dc converter as a function of the duty cycle; $V_{\text{pan}\,H}(V_{\text{pan}\,L})$, output voltage of a PV module with irradiation $SH(SL)$; $I_{\text{pan}\,H}(I_{\text{pan}\,L})$, output current of a module with irradiation $SH(SL)$; and $f(V_{\text{pan}})$, I–V characteristic of the PV module at a given temperature.

Equations (2)–(9) can be solved with respect to variables $V_{\text{out}\,H}$, $V_{\text{out}\,L}$, $I_{\text{out}\,H}$, $I_{\text{out}\,L}$, D_H, D_L, $I_{\text{pan}\,H}$, and $I_{\text{pan}\,L}$ for each assigned couple of values $V_{\text{pan}\,H}$ and $V_{\text{pan}\,L}$ belonging to the operating range of the PV module voltages. Voltage V_{LOAD} is fixed. Due to the series connection of SCPVM output ports, the output voltage of a given SCPVM is related to the ratio between its output power and the total output power

$$V_{\text{out}\,X} = V_{\text{LOAD}}\frac{P_{\text{out}\,X}}{HP_{\text{out}\,H} + LP_{\text{out}\,L}} \tag{10}$$

where $P_{\text{out}\,H}$ and $P_{\text{out}\,L}$ are the output powers of SCPVMs with irradiations SH and SL, respectively. Subscript X can stand for either H or L. Equation (10) highlights that the output voltage of an SCPVM can vary in a wide range due to possible imbalances among powers delivered by modules. If, for example, $P_{\text{out}\,L} \sim 0$ (the L modules are totally shadowed) while $P_{\text{out}\,H} \neq 0$, from (10), we get $V_{\text{out}\,L} \sim 0$ and $V_{\text{out}\,H} = V_{\text{LOAD}}/H$. Therefore, if H is sufficiently low, $V_{\text{out}\,H}$ can become very large, causing high switch stresses. Output voltage in a boost converter corresponds to the maximum voltage across the switches and the output capacitor. In order to prevent the output voltage of one or more SCPVMs from exceeding a given maximum value $V_{\text{ds max}}$, an output-voltage limitation technique must be adopted by means of a suitable duty-cycle limitation function, as shown in Fig. 3.

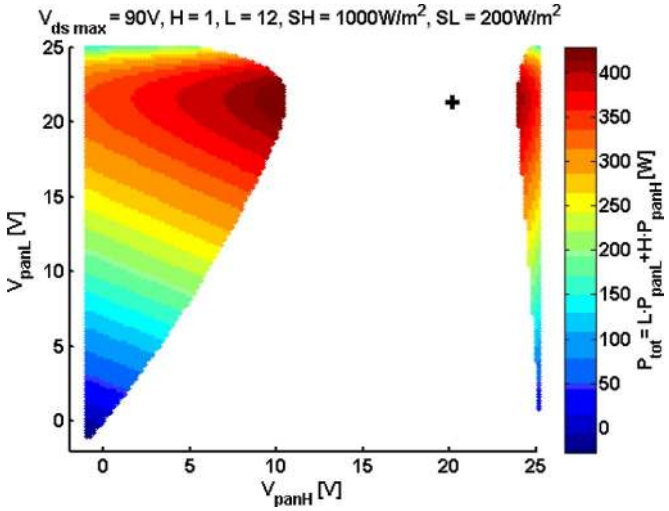

Fig. 5. Feasibility map of the system shown in Fig. 4 (boost topology; $V_{\text{ds max}} = 90$ V; black cross indicates global MPP).

The output-voltage limitation constraint is

$$V_{\text{out}\,X} \leq V_{\text{ds max}}. \tag{11}$$

Solution $[V_{\text{out}\,H}, V_{\text{out}\,L}, I_{\text{out}\,H}, I_{\text{out}\,L}, D_H, D_L, I_{\text{pan}\,H}, I_{\text{pan}\,L}]$ of (2)–(9) can be easily found for every assigned couple $(V_{\text{pan}\,H}, V_{\text{pan}\,L})$ under constraint (11). The couples of values of $V_{\text{pan}\,H}$ and $V_{\text{pan}\,L}$, which fulfill (2)–(9), and (11) and belong to the operating range of a given PV module, represent feasible operating points for the system. Feasible values of $V_{\text{pan}\,H}$ and $V_{\text{pan}\,L}$ can be plotted in a plane, leading to a map which represents the possible steady-state operating points of the system under given irradiation and temperature conditions. Figs. 5 and 6 show the maps of feasible points of the same DMPPT system for two different values of $V_{\text{ds max}}$. System output power is also plotted, for each feasible point, in a color scale. In the following, such plots will also be referred to as feasibility maps. System and environmental parameters adopted for the numerical solution of (2)–(9), and (11) are the following ones: PV module Kyocera 175 W; $H = 1$; $L = 12$; $SH = 1000$ W/m^2; $SL = 200$ W/m^2; $T_a = 300$ K (ambient temperature); nominal power of the module at SH, 147.5 W; nominal power of the module at SL, 29 W; $V_{\text{LOAD}} = 400$ V; and $R_{\text{LOAD}} = 0$.

Equations (2)–(9), and (11) show that feasibility maps of the system under given irradiance and thermal conditions depend not only on $V_{\text{ds max}}$ but also on converter's conversion ratio $M(D)$ and, thus, on its topology and efficiency, as well as inverter's input voltage V_{LOAD}. Figs. 5 and 6 show that,

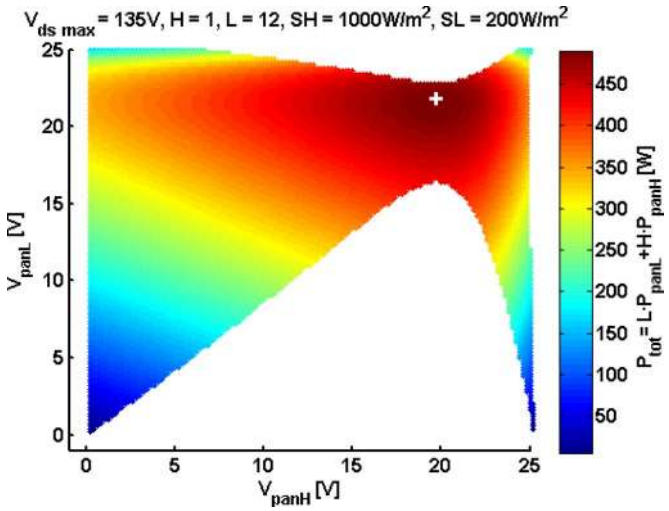

Fig. 6. Feasibility map of the system shown in Fig. 4 (boost topology; $V_{\mathrm{ds\ max}} = 135$ V; white cross indicates global MPP).

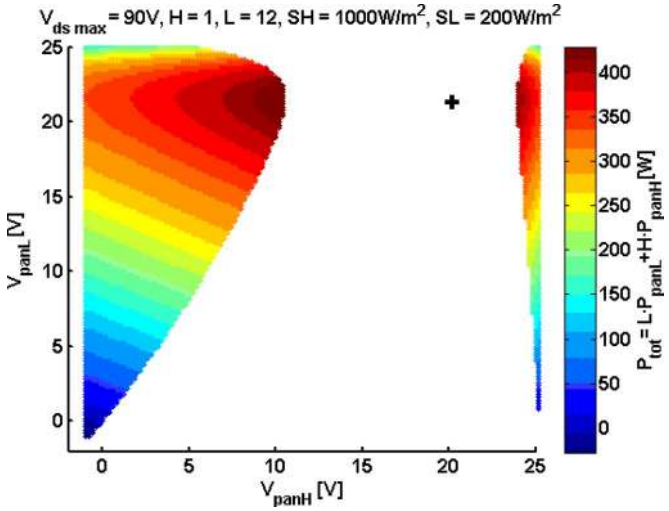

Fig. 7. Feasibility map of the system shown in Fig. 4 (buck–boost topology; $V_{\mathrm{ds\ max}} = 90$ V; black cross indicates global MPP).

depending on environmental conditions and system parameters, global MPP is not always achievable. Global MPP indeed corresponds to the couple $(V_{\mathrm{MPP}\,L}, V_{\mathrm{MPP}\,H})$, where $V_{\mathrm{MPP}\,L}$ is the MPP voltage of the shaded modules and $V_{\mathrm{MPP}\,H}$ is the MPP voltage of the fully illuminated modules.

Such a point is only achievable in the case shown in Fig. 6, whereas only a constrained MPP can be achieved in the case of Fig. 5. Figs. 7 and 8 show the feasibility maps of the same PV array when a buck–boost topology is employed in an SCPVM. $V_{\mathrm{ds\ max}}$ represents the maximum value of the voltage across the switches of the converter. Whereas, in the boost topology, the voltage across the active switch, during its off subinterval, is equal to the output voltage [10], and, in the case of the buck–boost topology, the voltage across the active switch, during its off subinterval, is equal to the sum of the input and output voltages [10], therefore, the quantity $V_{\mathrm{pan}\,X} + V_{\mathrm{out}\,X}$ has to be limited to the value $V_{\mathrm{ds\ max}}$, leading to smaller feasibility regions. Therefore, the choice of SCPVM configuration, as well as dc–dc converter topology and system parameter values,

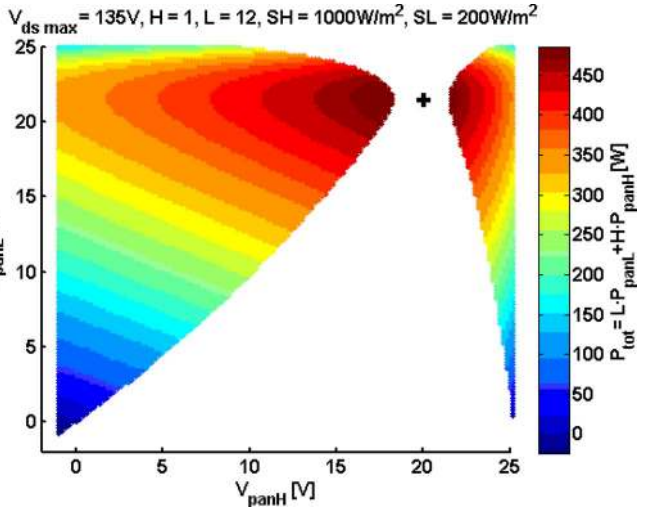

Fig. 8. Feasibility map of the system shown in Fig. 4 (buck–boost topology; $V_{\mathrm{ds\ max}} = 135$ V; black cross indicates global MPP).

strongly impacts system's performance. Feasibility maps can be used to properly design system parameters according to given performance specifications.

III. AC Model of a Single SCPVM

Fig. 9 shows the detailed schematic of the SCPVM under study, including the linear control network achieving input-voltage feedback regulation.

In the small-signal model of the system under study, the PV module is represented by a current source I_g and a parallel resistor R_{pan} whose values depend on the considered operating point. In the following, small letters like v, i, and d will be used to indicate the large signal value of voltages, currents, and duty cycle, respectively, whereas capital letters like V, I, and D will be used to indicate their dc values, and tilde small letters will indicate small-signal variations around their steady-state operating point.

Input-, output-, and state-variable vectors can be defined as follows:

input variables $\quad \underline{u} = [v_{\mathrm{LOAD}} \quad i_g \quad \mathrm{d}]^{\mathrm{T}}$;
output variables $\quad \underline{y} = [v_{\mathrm{pan}} \quad i_{\mathrm{out}}]^{\mathrm{T}}$;
state variables $\quad \underline{x} = [v_{C\,\mathrm{in}} \quad v_{C\,\mathrm{out}} \quad i_{L\,\mathrm{out}}]^{\mathrm{T}}$.

The following open-loop transfer functions can be defined to relate small-signal variations of input and output variables in the system of Fig. 9:

$$G_{v_{\mathrm{pan}}d\,\mathrm{OL}}(s) = \left.\frac{\tilde{v}_{\mathrm{pan}}(s)}{\tilde{d}(s)}\right|_{\substack{\tilde{i}_g=0\\ \tilde{v}_{\mathrm{LOAD}}=0\\ \text{open loop}}} \tag{12.a}$$

$$G_{i_{\mathrm{LOAD}}d\,\mathrm{OL}}(s) = \left.\frac{\tilde{i}_{\mathrm{LOAD}}(s)}{\tilde{d}(s)}\right|_{\substack{\tilde{i}_g=0\\ \tilde{v}_{\mathrm{LOAD}}=0\\ \text{open loop}}} \tag{12.b}$$

$$Z_{v_{\mathrm{pan}}i_g\,\mathrm{OL}}(s) = \left.\frac{\tilde{v}_{\mathrm{pan}}(s)}{\tilde{i}_g(s)}\right|_{\substack{\tilde{d}=0\\ \tilde{v}_{\mathrm{LOAD}}=0\\ \text{open loop}}} \tag{12.c}$$

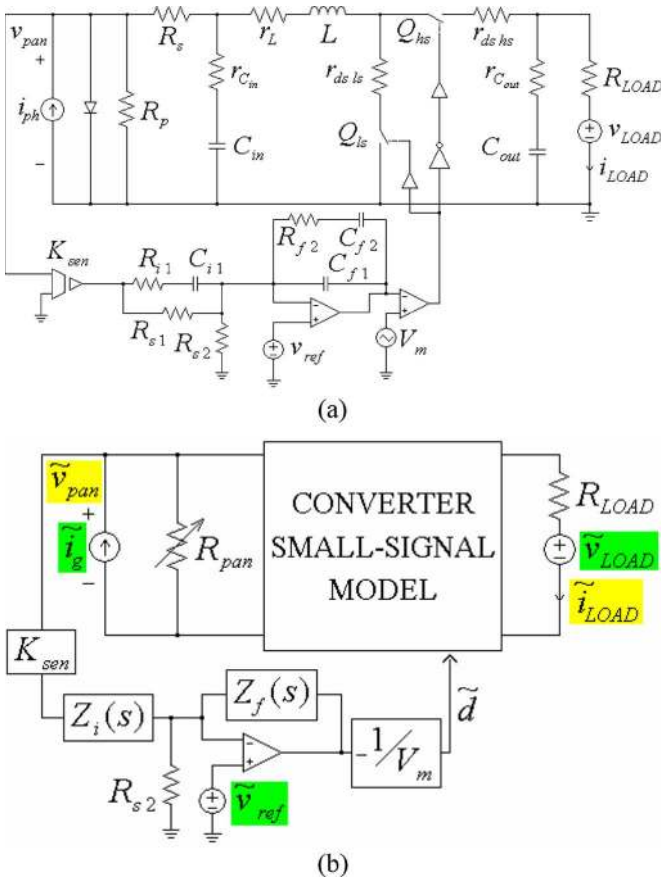

Fig. 9. (a) Schematic of the SCPVM under study (i_{ph}, R_p, and R_s are the parameters of the large-signal model of the PV module). (b) Small-signal model of the system under study. Green: Input variables. Yellow: Output variables.

$$G_{i_{\mathrm{LOAD}} i_g\,\mathrm{OL}}(s) = \left.\frac{\tilde{i}_{\mathrm{LOAD}}(s)}{\tilde{i}_g(s)}\right|_{\substack{\tilde{d}=0 \\ \tilde{v}_{\mathrm{LOAD}}=0 \\ \text{open loop}}} \tag{12.d}$$

$$G_{v_{\mathrm{pan}} v_{\mathrm{LOAD}}\,\mathrm{OL}}(s) = \left.\frac{\tilde{v}_{\mathrm{pan}}(s)}{\tilde{v}_{\mathrm{LOAD}}(s)}\right|_{\substack{\tilde{i}_g=0 \\ \tilde{d}=0 \\ \text{open loop}}} \tag{12.e}$$

$$Z_{\mathrm{out\,OL}}(s) = -\left.\frac{\tilde{v}_{\mathrm{LOAD}}(s)}{\tilde{i}_{\mathrm{LOAD}}(s)}\right|_{\substack{\tilde{i}_g=0 \\ \tilde{d}=0 \\ \text{open loop}}}. \tag{12.f}$$

The loop transfer function can be written as

$$T_c(s) = -G_{v_{\mathrm{pan}} d\,\mathrm{OL}}(s) K_{\mathrm{sen}} G_c(s) \frac{1}{V_m} \tag{13}$$

where K_{sen} is the gain of the input-voltage sensor and $G_c(s) = (Z_f(s)/Z_i(s))$, with $Z_f(s) = (R_{f2} + (1/sC_{f2}))\|(1/sC_{f1})$ and $Z_i(s) = (R_{i1} + (1/sC_{i1}))\|R_{s1}$.

The negative sign in (13) is introduced in the circuit by the negative pulsewidth-modulation block of Fig. 9. This is due to the fact that the transfer function $G_{v_{\mathrm{pan}} d\,\mathrm{OL}}(s)$ is negative at low frequencies, and therefore, it is necessary to introduce a negative sign in the feedback loop to have a stable closed-loop function.

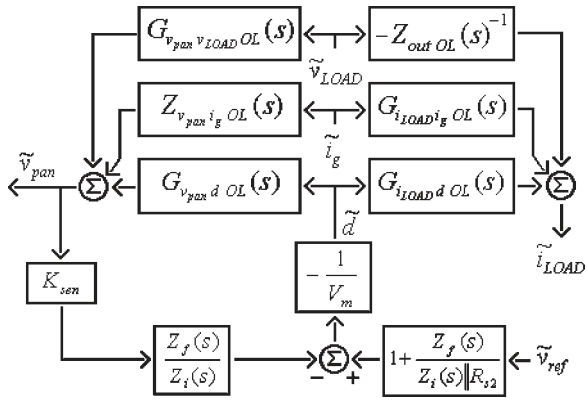

Fig. 10. Block scheme of the small-signal ac model of the circuit in Figs. 3 and 9.

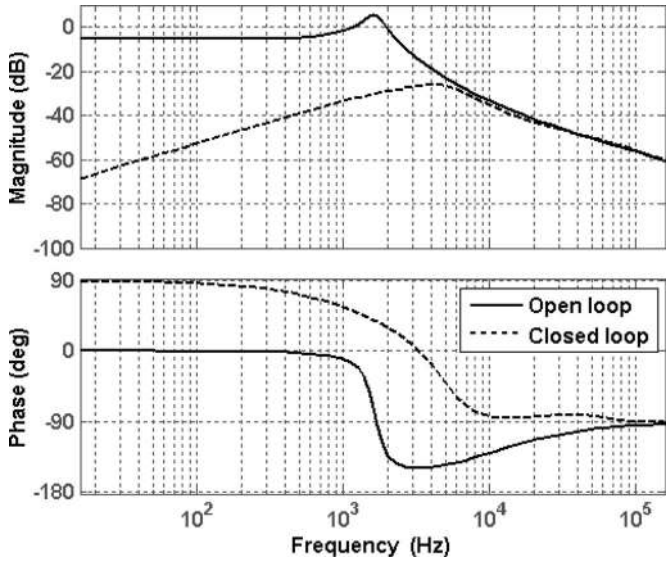

Fig. 11. Output-to-input voltage transfer function $G_{v_{\mathrm{pan}} v_{\mathrm{LOAD}}}(s)$ of the circuit of Figs. 3 and 9 in (solid line) open-loop and (dashed line) closed-loop conditions.

The block diagram of Fig. 10 schematizes the dynamic interactions between input and output variables of the SCPVM.

The closed-loop transfer functions of the SCPVM can be computed from the open-loop transfer functions of (14)–(19), shown at the bottom of the next page.

Fig. 11 shows the Bode plots of the transfer functions $G_{v_{\mathrm{pan}} v_{\mathrm{LOAD}}\mathrm{OL}}(s)$ and $G_{v_{\mathrm{pan}} v_{\mathrm{LOAD}}\mathrm{CL}}(s)$. It is worth noting that, as it is well known [8], in grid-connected PV system, voltage oscillations at a frequency which is the double of the grid frequency take place at the inverter-input terminals. Such oscillations propagate to the PV array terminals, leading to a consistent decrease of the efficiency of the overall system. In fact, not only that the operating point of the PV array is forced to oscillate more or less far from the MPP but also that the MPPT algorithm can be confused, leading to an additional waste of available energy. In order to almost totally remove the oscillations of the PV voltage caused by the oscillations of the voltage at the inverter input, it is mandatory to obtain a sufficiently low magnitude of the output-to-input-voltage transfer

function $G_{v_{\rm pan}v_{\rm LOAD}{\rm CL}}(s)$ [8]. Due to the output-voltage disturbance rejection feature shown in Fig. 11 by $G_{v_{\rm pan}v_{\rm LOAD}{\rm CL}}(s)$, compared with $G_{v_{\rm pan}v_{\rm LOAD}OL}(s)$, it is possible to state that the MPPT performances of the SCPVM in closed loop are greatly enhanced with respect to the case of the same system operating in open loop.

The values of parameters used to plot such Bode diagrams have been determined by using the procedure described in [8], [10], and [20] and are listed as follows: $L = 100\ \mu$H, $r_L = 0.082\ \Omega$, $r_{\rm ds\_hs} = 0.021\ \Omega$, $r_{\rm ds\_ls} = 0.013\ \Omega$, $C_{\rm out} = 99\ \mu$F, $r_{C\,\rm out} = 0.12\ \Omega$, $C_{\rm in} = 94\ \times 10^{-6}$ F, $r_{C\,\rm in} = 0.18\ \Omega$, $f_s = 160$ kHz, $V_f = 0.6$ V, $R_{s1} = 1$ k Ω, $R_{s2} = 0.39$ kΩ, $R_{i1} = 100\,\Omega$, $C_{i1} = 47$ nF, $C_{f1} = 2.2$ nF, $R_{f2} = 1\,$kΩ, $C_{f2} = 47$ nF, $K_{\rm sen} = 0.454$, $V_m = 1.8$ V, $V_{\rm LOAD} = 27.5$ V, $R_{\rm LOAD} = 1\ m\Omega$, irradiance $= 500$ W/m^2, $V_{\rm pan} = 15$ V, $I_g = 4$ A, and $R_{\rm pan} = 84\,\Omega$.

IV. AC Model of a String of SCPVMs

In this paragraph, an AC model is derived for the system of Fig. 4. The case $H = L = 1$ is considered for simplicity. The resulting small-signal model is shown in Fig. 12. Input and output variables for the system of Fig. 12 are defined similarly to the case of a single module system of Fig. 9 and are listed below:

input variables $\quad i_{g\,1}, i_{g\,2}, v_{\rm ref\,1}, v_{\rm ref\,2}, v_{\rm LOAD}$;
output variables $\quad v_{\rm pan\,1}, v_{\rm pan\,2}$.

The resulting small-signal model is shown in Fig. 12. The following transfer functions relate $v_{\rm pan\,1}$ to the input variables:

$$G_{v_{\rm pan\,1}v_{\rm ref\,1}{\rm SYS}}(s) = \left.\frac{\tilde{v}_{\rm pan\,1}(s)}{\tilde{v}_{\rm ref\,1}(s)}\right|_{\substack{\tilde{v}_{\rm LOAD}(s)=0\\ \tilde{v}_{\rm ref\,2}(s)=0\\ \tilde{i}_{g\,1}(s)=0\\ \tilde{i}_{g\,2}(s)=0}} \tag{20.a}$$

$$G_{v_{\rm pan\,1}v_{\rm ref\,2}{\rm SYS}}(s) = \left.\frac{\tilde{v}_{\rm pan\,1}(s)}{\tilde{v}_{\rm ref\,2}(s)}\right|_{\substack{\tilde{v}_{\rm LOAD}(s)=0\\ \tilde{v}_{\rm ref\,1}(s)=0\\ \tilde{i}_{g\,1}(s)=0\\ \tilde{i}_{g\,2}(s)=0}} \tag{20.b}$$

$$Z_{v_{\rm pan\,1}i_{g\,1}{\rm SYS}}(s) = \left.\frac{\tilde{v}_{\rm pan\,1}(s)}{\tilde{i}_{g\,1}(s)}\right|_{\substack{\tilde{v}_{\rm LOAD}(s)=0\\ \tilde{v}_{\rm ref\,1}(s)=0\\ \tilde{v}_{\rm ref\,2}(s)=0\\ \tilde{i}_{g\,2}(s)=0}} \tag{20.c}$$

$$Z_{v_{\rm pan\,1}i_{g\,2}{\rm SYS}}(s) = \left.\frac{\tilde{v}_{\rm pan\,1}(s)}{\tilde{i}_{g\,2}(s)}\right|_{\substack{\tilde{v}_{\rm LOAD}(s)=0\\ \tilde{v}_{\rm ref\,1}(s)=0\\ \tilde{v}_{\rm ref\,2}(s)=0\\ \tilde{i}_{g\,1}(s)=0}} \tag{20.d}$$

$$G_{v_{\rm pan\,1}v_{\rm LOAD}{\rm SYS}}(s) = \left.\frac{\tilde{v}_{\rm pan\,1}(s)}{\tilde{v}_{\rm LOAD}(s)}\right|_{\substack{\tilde{v}_{\rm ref\,1}(s)=0\\ \tilde{v}_{\rm ref\,2}(s)=0\\ \tilde{i}_{g\,1}(s)=0\\ \tilde{i}_{g\,2}(s)=0}}. \tag{20.e}$$

Transfer functions relating $v_{\rm pan\,2}$ to input variables can be defined similarly. The transfer functions defined earlier can be derived from the transfer functions of a single SCPVM

$$G_{v_{\rm pan}v_{\rm ref}{\rm CL}}(s) = \left.\frac{\tilde{v}_{\rm pan}}{\tilde{v}_{\rm ref}}\right|_{\substack{\tilde{i}_g=0\\ \tilde{v}_{\rm LOAD}=0\\ \text{closed loop}}} = -\frac{\left[1+\frac{Z_f(s)}{Z_i(s)\|R_{s2}}\right]\frac{G_{v_{\rm pan}d\,\rm OL}(s)}{V_m}}{1+T_c(s)} \tag{14}$$

$$G_{i_{\rm LOAD}v_{\rm ref}{\rm CL}}(s) = \left.\frac{\tilde{i}_{\rm LOAD}}{\tilde{v}_{\rm ref}}\right|_{\substack{\tilde{i}_g=0\\ \tilde{v}_{\rm LOAD}=0\\ \text{closed loop}}} = -\frac{\left[1+\frac{Z_f(s)}{Z_i(s)\|R_{s2}}\right]\frac{G_{i_{\rm LOAD}d\,\rm OL}(s)}{V_m}}{1+T_c(s)} \tag{15}$$

$$G_{v_{\rm pan}v_{\rm LOAD}{\rm CL}}(s) = \left.\frac{\tilde{v}_{\rm pan}}{\tilde{v}_{\rm LOAD}}\right|_{\substack{\tilde{i}_g=0\\ \tilde{v}_{\rm ref}=0\\ \text{closed loop}}} = \frac{G_{v_{\rm pan}v_{\rm LOAD}{\rm OL}}(s)}{1+T_c(s)} \tag{16}$$

$$Z_{\rm out\,CL}(s) = -\left.\frac{\tilde{v}_{\rm LOAD}}{\tilde{i}_{\rm LOAD}}\right|_{\substack{\tilde{i}_g=0\\ \tilde{v}_{\rm ref}=0\\ \text{closed loop}}} = \frac{Z_{\rm out\,OL}(s)}{1-\frac{Z_{\rm out\,OL}(s)G'(s)}{1+T_c(s)}} \tag{17.1}$$

$$G'(s) = G_{i_{\rm LOAD}d\,\rm OL}(s)G_{v_{\rm pan}v_{\rm LOAD}{\rm OL}}(s)K_{\rm sen}G_c(s)\frac{1}{V_m} \tag{17.2}$$

$$G_{i_{\rm LOAD}i_g{\rm CL}}(s) = \left.\frac{\tilde{i}_{\rm LOAD}}{\tilde{i}_g}\right|_{\substack{\tilde{v}_{\rm LOAD}=0\\ \tilde{v}_{\rm ref}=0\\ \text{closed loop}}} = G_{i_{\rm LOAD}i_g{\rm OL}}(s) + \frac{G_{i_{\rm LOAD}d\,\rm OL}(s)Z_{v_{\rm pan}i_g{\rm OL}}(s)K_{\rm sen}\frac{G_c(s)}{V_m}}{1+T_c(s)} \tag{18}$$

$$Z_{v_{\rm pan}i_g{\rm CL}}(s) = \left.\frac{\tilde{v}_{\rm pan}}{\tilde{i}_g}\right|_{\substack{\tilde{v}_{\rm LOAD}=0\\ \tilde{v}_{\rm ref}=0\\ \text{closed loop}}} = \frac{Z_{v_{\rm pan}i_g{\rm OL}}(s)}{1+T_c(s)} \tag{19}$$

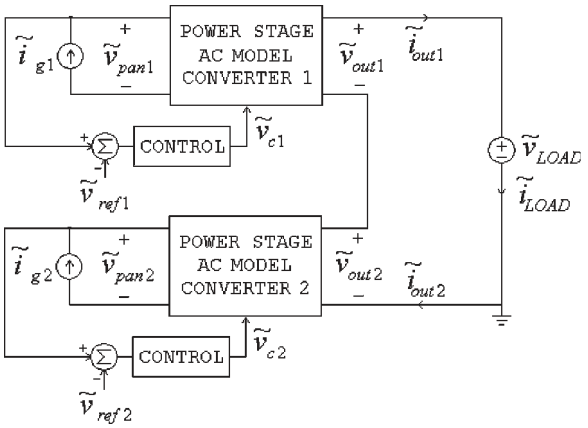

Fig. 12. Interconnection of blocks representing the linear models of SCPVMs of Fig. 4.

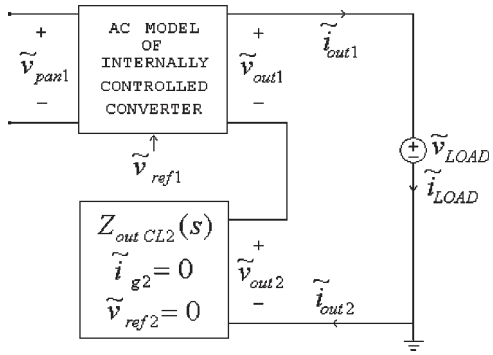

Fig. 13. Application of Middlebrook's extra element theorem to the system of Fig. 12.

by applying Middlebrook's extra element theorem [10] and the properties of cascaded linear systems. As an example, the application of Middlebrook's theorem gives

$$G_{v_{\rm pan\,1}v_{\rm ref\,1}{\rm SYS}}(s) = G_{v_{\rm pan}v_{\rm ref}{\rm CL\,1}}(s)\frac{1+\frac{Z_{\rm out\,CL\,2}(s)}{Z_{N\,{\rm CL\,1}}(s)}}{1+\frac{Z_{\rm out\,CL\,2}(s)}{Z_{D\,{\rm CL\,1}}(s)}} \quad (21)$$

where $Z_{\rm out\,CL2}(s)$ is the closed-loop output impedance of SCPVM 2, as shown in Fig. 13, and $G_{v_{\rm pan}v_{\rm ref}{\rm CL\,1}}(s)$ is the $v_{\rm ref}$-to-$v_{\rm pan}$ transfer function of SCPVM 1 as previously defined.

Impedances $Z_{N\,{\rm CL}\,i}(s)$ and $Z_{D\,{\rm CL}\,i}(s)$ are defined as follows:

$$Z_{D\,{\rm CL}\,i}(s) = -\left.\frac{\tilde{v}_{{\rm out}\,i}(s)}{\tilde{i}_{{\rm out}\,i}(s)}\right|_{\substack{\tilde{v}_{{\rm ref}\,i}(s)=0\\ \tilde{i}_{gi}(s)=0\\ \text{closed loop}}} \quad (22)$$

$$Z_{N\,{\rm CL}\,i}(s) = -\left.\frac{\tilde{v}_{{\rm out}\,i}(s)}{\tilde{i}_{{\rm out}\,i}(s)}\right|_{\substack{\tilde{v}_{{\rm pan}\,i}(s)\to 0\\ \tilde{i}_{gi}(s)=0\\ \text{closed loop}}} \quad (23)$$

$$Z_{D\,{\rm CL}\,i}(s) = Z_{{\rm out\,CL}\,i}(s) \quad (24)$$

$$Z_{N\,{\rm CL}\,i}(s) = \frac{Z_{{\rm out\,CL}\,i}(s)}{1+\frac{Z_{{\rm out\,CL}\,i}(s)}{1+T_c(s)}\frac{G_{v_{\rm pan}v_{\rm LOAD}{\rm OL}\,i}(s)G_{i_{\rm LOAD}d\,{\rm OL}\,i}(s)}{G_{v_{\rm pan}d\,{\rm OL}\,i}(s)}}. \quad (25)$$

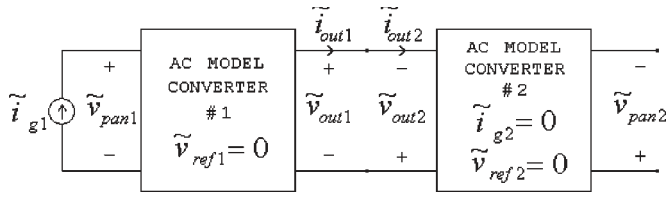

Fig. 14. Application of the superposition principle of linear systems to the system of Fig. 12.

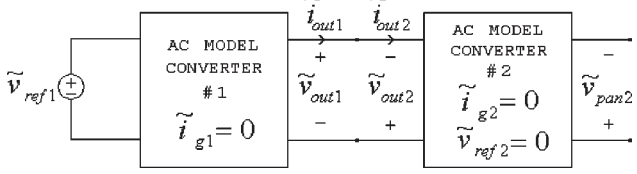

Fig. 15. Application of the superposition principle of linear systems to the system of Fig. 12.

To derive the transfer function $Z_{v_{\rm pan\,2}i_{g\,1}{\rm SYS}}(s)$, we can refer to the cascade interconnection of two-port systems shown in Fig. 14 [21].

For the system in Fig. 14, it is

$$Z_{v_{\rm pan\,2}i_{g\,1}{\rm SYS}}(s) = -\frac{G_{i_{\rm LOAD}i_g{\rm CL\,1}}(s)G_{v_{\rm pan}v_{\rm LOAD}{\rm CL\,2}}(s)Z_{\rm out\,CL\,2}(s)}{1+\frac{Z_{\rm out\,CL\,2}(s)}{Z_{\rm out\,CL\,1}(s)}}. \quad (26)$$

The transfer function $G_{v_{\rm pan\,2}v_{\rm ref\,1}{\rm SYS}}(s)$ can be derived similarly by considering the cascade interconnection of two-port systems shown in Fig. 15, leading to

$$G_{v_{\rm pan\,2}v_{\rm ref\,1}{\rm SYS}}(s) = -\frac{G_{i_{\rm LOAD}v_{\rm ref}{\rm CL\,1}}(s)G_{v_{\rm pan}v_{\rm LOAD}{\rm CL\,2}}(s)Z_{\rm out\,CL\,2}(s)}{1+\frac{Z_{\rm out\,CL\,2}(s)}{Z_{\rm out\,CL\,1}(s)}}. \quad (27)$$

Finally, in a similar way, it is possible to obtain

$$G_{v_{\rm pan\,1}v_{\rm LOAD}{\rm SYS}}(s) = \frac{G_{v_{\rm pan}v_{\rm LOAD}{\rm CL\,1}}(s)Z_{\rm out\,CL\,1}(s)}{Z_{\rm out\,CL\,1}(s)+Z_{\rm out\,CL\,2}(s)}. \quad (28)$$

Stability of the system of Fig. 12 can be predicted by deriving the loop transfer function of each one of the converters and applying Middlebrook's extra element theorem. In fact, if one is able to get the closed-form expression of the loop gain of each SCPVM, by taking into account the role played by the other SCPVMs belonging to the string, then it is possible to apply classical stability criteria (e.g., the phase margin test [10]) by analyzing such a loop gain. The loop transfer function of SCPVM 1 in Fig. 12 is

$$T_{c\,1\,{\rm SYS}}(s) = G_{v_{\rm pan\,1}d_1\,{\rm SYS}}(s)K_{\rm sen}G_c(s)\frac{1}{V_m} \quad (29)$$

where

$$G_{v_{\rm pan\,1}d_1\,{\rm SYS}}(s) = G_{v_{\rm pan}d\,{\rm OL\,1}}(s)\frac{1+\frac{Z_{\rm out\,CL\,2}(s)}{Z_{N\,{\rm OL\,1}}(s)}}{1+\frac{Z_{\rm out\,CL\,2}(s)}{Z_{D\,{\rm OL\,1}}(s)}} \quad (30)$$

and the terms $Z_{N\,\mathrm{OL}\,i}(s)$ and $Z_{D\,\mathrm{OL}\,i}(s)$ can be derived likewise with the terms $Z_{N\,\mathrm{CL}\,i}(s)$ and $Z_{D\,\mathrm{CL}\,i}(s)$ in (22)–(25) leading to

$$Z_{D\,\mathrm{OL}\,i}(s) = Z_{\mathrm{out}\,\mathrm{OL}\,i}(s) \tag{31}$$

$$Z_{N\,\mathrm{OL}\,i}(s) = \frac{Z_{\mathrm{out}\,\mathrm{OL}\,i}(s)}{1 + \frac{G_{v_{\mathrm{pan}}v_{\mathrm{LOAD}}\mathrm{OL}\,i}(s) G_{i_{\mathrm{LOAD}}d\,\mathrm{OL}\,i}(s) Z_{\mathrm{out}\,\mathrm{OL}\,i}(s)}{G_{v_{\mathrm{pan}}d\,\mathrm{OL}\,i}(s)}}. \tag{32}$$

Bode or Nyquist criteria can be applied to the transfer function $T_{c\,1\,\mathrm{SYS}}(s)$. However, to predict stability of the system of Fig. 12, such criteria must be satisfied for all SCPVMs in all the possible mismatching operating conditions. In principle, if $Z_{N\,\mathrm{OL}\,1} \gg Z_{\mathrm{out}\,\mathrm{CL}\,2}$ and $Z_{D\,\mathrm{OL}\,1} \gg_{Z_{\mathrm{out}\,\mathrm{CL}\,2}}$, the loop function of converter 1 is not affected by the operation of converter 2. This condition is not easy to be ensured because the transfer function $Z_{\mathrm{out}\,\mathrm{CL}\,2}$ depends entirely on converter 2. Moreover, in the general case of a string composed by N SCPVMs, (30) would assume the following form:

$$G_{v_{\mathrm{pan}\,1}d_1\,\mathrm{SYS}}(s) = G_{v_{\mathrm{pan}}d\,\mathrm{OL}\,1}(s) \frac{1 + \frac{\sum_{i=2}^{N} Z_{\mathrm{out}\,\mathrm{CL}\,i}(s)}{Z_{N\,\mathrm{OL}\,1}(s)}}{1 + \frac{\sum_{i=2}^{N} Z_{\mathrm{out}\,\mathrm{CL}\,i}(s)}{Z_{D\,\mathrm{OL}\,1}(s)}}. \tag{33}$$

From the analysis of (33), it is evident that, if $Z_{N\,\mathrm{OL}\,1}$ was perfectly equal to $Z_{D\,\mathrm{OL}\,1}$ (and hence $G_{v_{\mathrm{pan}\,1}d_1\,\mathrm{SYS}}(s) = G_{v_{\mathrm{pan}}d\,\mathrm{OL}\,1}(s)$), then the loop function of SCPVM 1 would not be influenced at all by the presence of the remaining SCPVMs, whichever their number is. In this case, the stability of SCPVM 1 could be predicted *a priori*, ignoring the number of SCPVMs connected in series and their properties. In general, however, because the equality $Z_{N\,\mathrm{OL}\,1} = Z_{D\,\mathrm{OL}\,1}$ is not fulfilled, the effect of the presence of the remaining SCPVMs in the string on the operation of SCPVM 1 must be taken into account. Such an effect, however, can be made negligible as long as $Z_{N\,\mathrm{OL}\,1} \approx Z_{D\,\mathrm{OL}\,1}$.

For the system under study, condition $Z_{N\,\mathrm{OL}\,1} \approx Z_{D\,\mathrm{OL}\,1}$ is verified in a wide range of frequencies. In fact, as it will be clarified later on, the system of Fig. 2 has been analyzed by the authors in a wide range of shade intensities and number of shaded panels, and stability has never been found to be dramatically affected by module interaction. Fig. 16 shows the transfer functions $T_{c\,H}(s)$, $T_{c\,L}(s)$ [given by (13)], and $T_{c\,H\,\mathrm{SYS}}(s)$, $T_{c\,L\,\mathrm{SYS}}(s)$ [given by (29)] in correspondence of the following operating conditions: $H = 1$, $L = 12$, $SH = 1000$ W/m^2, $SL = 500$ W/m^2, $V_{\mathrm{pan}\,H} = 19.8$ V, $V_{\mathrm{pan}\,L} = 15$ V, $I_{g\,H} = 11$ A, $I_{g\,L} = 4$ A, $R_{\mathrm{pan}\,H} = 2.6\ \Omega$, $R_{pan\,L} = 84\ \Omega$, (converter parameters as those ones used to draw the Bode plots of Fig. 11). The effect of the series interconnection is negligible around the crossover frequency, or it is not strong enough to affect stability and dynamic performances of each SCPVM when operating in a series configuration. Consequently, if each MPPT controller introduces a perturbation of the control variable at a frequency which is much lower than the crossover frequencies of $T_c(s)$ and $T_{c\,\mathrm{SYS}}(s)$, not only each SCPVM will be able to regulate its voltage V_{pan} to a reference value imposed by its own MPPT controller but also, at the same time, the MPPT controller of a specific SCPVM will not involve any additional dynamic effect on the other SCPVMs. This means that, if the global MPP belongs to the feasibility map of the system, in that operating condition, the DMPPT will be able to achieve it.

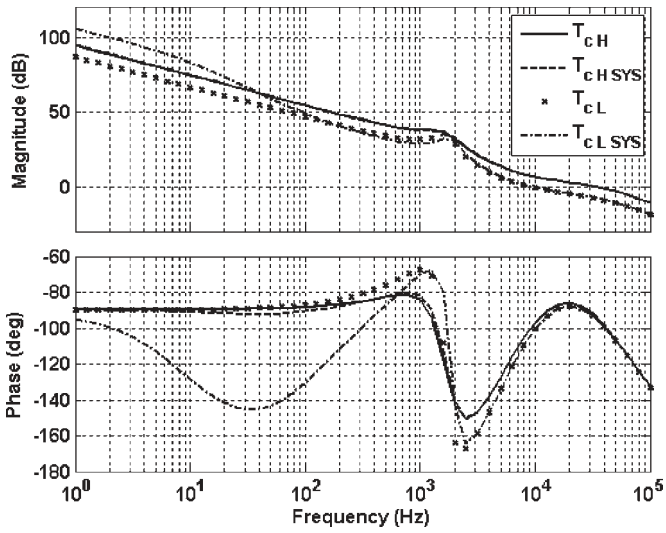

Fig. 16. Loop transfer functions of the SCPVMs of Fig. 2 as (solid and x-marked lines) isolated systems and as (dashed and dashed–dotted lines) part of the interconnected system.

The effect of module interconnection has been investigated via analytic results and system simulation. A string of 13 SCPVMs, with a number of shaded modules ranging from 2 to 12 and an irradiation of the shaded modules ranging from 20% to 80% of the full irradiation, has been considered. In all the cases, it has been found that the string of SCPVMs is stable. This result can be justified by considering that the transfer function $G_{v_{\mathrm{pan}}d\,\mathrm{OL}}(s)$ does not contain the right-half-plane zero which is typical of the boost converter with output-voltage control, and as a consequence, it is not characterized by an intrinsically low phase. The loop transfer function of the boost converter with input-voltage control is very similar to the corresponding one of the buck converter with output-voltage control. This aspect represents an additional advantage of the adoption of the boost topology with respect to other topologies (such as the buck–boost or higher order topologies) which may instead lead to stability problems.

V. Numerical Simulations

The system described in Section II has been simulated in a number of different operating conditions in the PSIM environment. Simulations have been carried out considering a string of 13 SCPVMs, with a number of shaded modules ranging from 2 to 12 and an irradiation of the shaded modules equal to 20%, 50%, and 80% of the full irradiation. The time step adopted to carry out the time-domain numerical simulations has been chosen to be equal to 1/150 of the switching period (switching frequency is 160 kHz); in each considered case, the adopted total simulation time is longer than the settling time needed to bring the system to steady-state operation. Power stage, compensation network, and load parameters are those ones

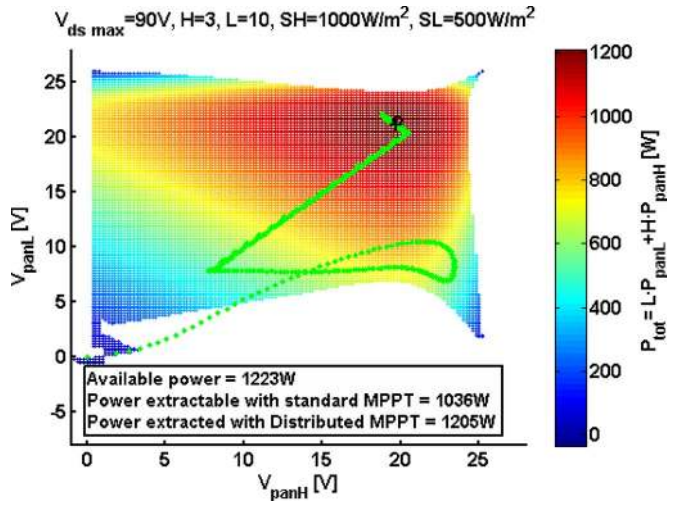

Fig. 17. (Green) Simulation data mapped on the feasibility map of the system. (Black cross) Steady-state operation coincides with (black circle) MPP.

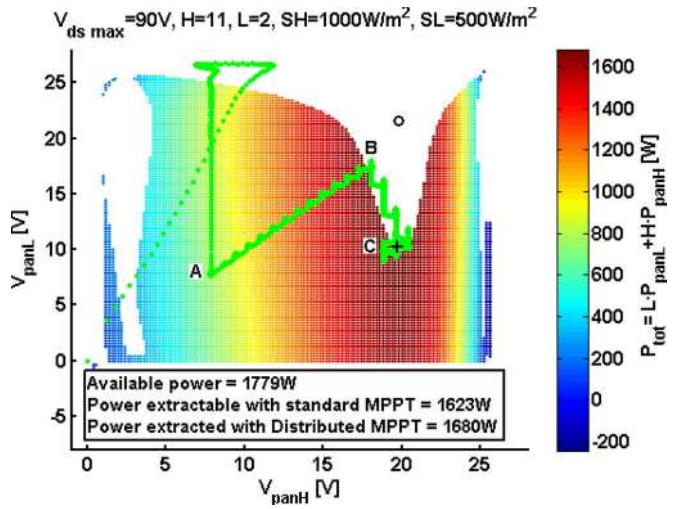

Fig. 18. (Green) Simulation data mapped on the feasibility map of the system. (Black cross) Steady-state operation corresponds to a constrained MPP. (Black circle) Global MPP is not a feasible point of the system.

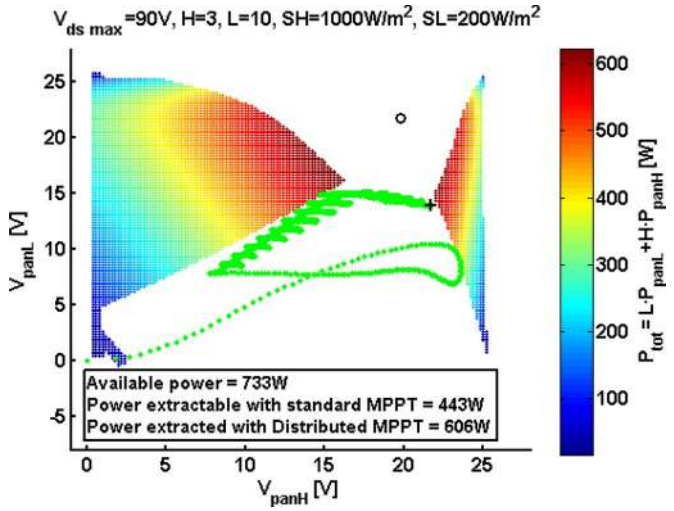

Fig. 19. (Green) Simulation data mapped on the feasibility map of the system. (Black cross) Steady-state operation corresponds to a constrained MPP. (Black circle) Global MPP is not a feasible point of the system.

reported in the previous sections. The adopted P&O parameters are as follows:

$\Delta V_{\rm ref} = 0.08\,{\rm V}$ amplitude of reference voltage perturbation;
$T_{\rm sample} = 0.002\,{\rm s}$ sampling interval.

Their values have been chosen on the basis of the rules discussed in [20]. Figs. 17–19 show time-domain simulation data mapped on the corresponding feasibility maps derived by solving (2)–(9), and (11) in two different environmental conditions. In Figs. 17–19, the *available power* represents the sum of the maximum powers of the different modules; the *power extractable with standard MPPT* represents the power that is extractable by a PV field composed of a unique string of N PV modules, equipped with bypass diodes, and by assuming that the MPPT technique is able to locate the absolute MPP among the various relative MPPs which may appear in mismatching conditions (indeed, it is well known that, in presence of mismatching operating conditions, standard MPPT techniques often fail the tracking of the global MPP); whereas the *power extracted with distributed MPPT* represents the power obtained by the PV field when adopting a unique string of N SCPVMs, as shown in Fig. 4.

In particular, Figs. 18 and 19 refer to cases in which the global MPP does not belong to the set of feasible points of the system. In these cases, the P&O algorithm gradually increases panels' voltage until duty-cycle limitation takes over. Such a condition corresponds to the instant when the trajectory of the system in the feasibility map hits the boundary of a feasible region. It is worth noting that the trajectories are not fully contained in the feasibility regions because these last are representative of steady-state operation, whereas trajectories refer to the instantaneous behavior of the transient startup of the system. The peculiar shape of the trajectories is due to the combined effects of MPPT and duty-cycle limitation. It is worth noting that, when a subset of SCPVMs operates with a limited duty cycle, as it happens in Figs. 18 and 19, the analysis described in Section IV, which instead refers to cases like the one shown in Fig. 17, must be modified. In fact, SCPVMs working under duty-cycle limitation must be considered as operating in open loop with a fixed duty cycle. System stability can be analyzed by applying the same approach proposed in the previous section but using, for each SCVPM, the appropriate transfer functions.

Simulation results can be used to carry out an efficiency comparison between standard MPPT and DMPPT. Table I collects the values given by the ratio between the *power extractable with standard MPPT* or *with DMPPT* and the *available power*, which are obtained in different cases. The efficiency of DMPPT is always higher than the corresponding one of standard MPPT.

Fig. 20 shows the time-domain waveforms of the PV voltages and the values of D_H and D_L, which correspond to the case shown in Fig. 18. In this case, the duty cycle D_L of the SCPVMs under the low irradiation value SL remains fixed to the lowest allowed value (0.1). In fact, in the case under study, a conversion ratio that is smaller than one would be

TABLE I
EFFICIENCY COMPARISON BETWEEN STANDARD MPPT AND DMPPT. SYSTEM PARAMETERS AS IN SIMULATIONS OF FIGS. 17–19

Standard MPPT efficiency				
S_L/S_H / L/N	200/1000	500/1000	800/1000	1000/1000
12/13	0,75	0,92	0,97	0,99
10/13	0,52	0,83	0,95	0,99
8/13	0,40	0,76	0,93	0,99
6/13	0,33	0,71	0,92	0,99
4/13	0,88	0,78	0,91	0,99
2/13	0,94	0,89	0,91	0,99

DMPPT efficiency				
S_L/S_H / L/N	200/1000	500/1000	800/1000	1000/1000
12/13	0,88	0,98	0,98	0,99
10/13	0,83	0,98	0,98	0,99
8/13	0,75	0,98	0,98	0,99
6/13	0,84	0,99	0,98	0,99
4/13	0,91	0,97	0,98	0,99
2/13	0,95	0,94	0,98	0,99

required by the shaded SCPVMs, but the lowest value of the conversion ratio characterizing the boost topology (equal to one) is obtained when the duty cycle approaches zero. That is why, the duty cycle assumes the saturated low value. In the case of Fig. 20, the L shaded SCPVMs operate in open-loop condition, and (33) can be written as

$$G_{v_{\mathrm{pan}\,1}d_1\mathrm{SYS}}(s) = G_{v_{\mathrm{pan}}d\,\mathrm{OL}\,1}(s)\frac{1+\frac{\sum_{i=2}^{H}Z_{\mathrm{out\,CL}\,i}(s)+\sum_{i=H+1}^{H+L}Z_{\mathrm{out\,OL}\,i}(s)}{Z_{N\,\mathrm{OL}\,1}(s)}}{1+\frac{\sum_{i=2}^{H}Z_{\mathrm{out\,CL}\,i}(s)+\sum_{i=H+1}^{H+L}Z_{\mathrm{out\,OL}\,i}(s)}{Z_{D\,\mathrm{OL}\,1}(s)}}. \quad (34)$$

When writing (34), the SCPVMs have been ordered such that those ones with indices from one to H are characterized by the irradiation level SH, whereas those ones with indices from $H+1$ to $H+L$ are characterized by the irradiation level SL and operate under duty-cycle limitation with a fixed duty cycle that is equal to D_L.

The resulting loop transfer functions $T_{c\,H}(s)$ and $T_{c\,H\,\mathrm{SYS}}(s)$ are shown in Fig. 21. They have been obtained with the following parameters: $H = 11$, $L = 2$, $SH = 1000$ W/m^2, $SL = 500$ W/m^2, $V_{\mathrm{pan}\,H} = 19.8$ V, $V_{\mathrm{pan}\,L} = 10$ V, $I_{g\,H} = 14.9$ A, $I_{g\,L} = 4.1$ A, $R_{\mathrm{pan}\,H} = 2.65\ \Omega$, $R_{\mathrm{pan}\,L} = 100\ \Omega$, (converter

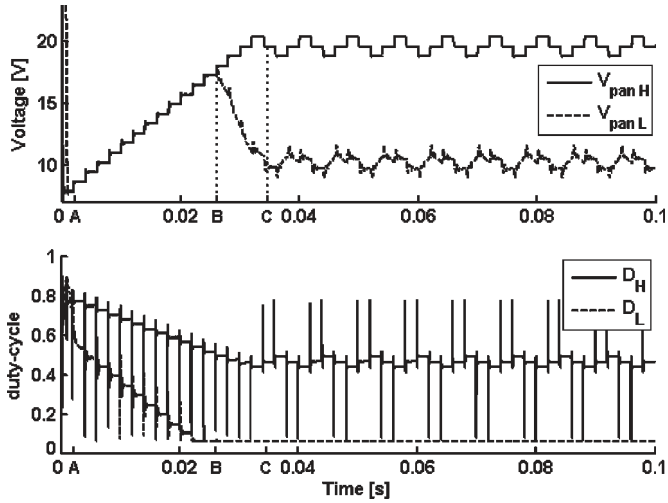

Fig. 20. Time-domain plots of the variables $V_{\mathrm{pan}\,H}$ and $V_{\mathrm{pan}\,L}$ and related duty cycles in the case shown in Fig. 18. While sliding on the boundary of the feasibility region, D_L equals the lower saturation value. Points A, B, and C correspond to points A, B, and C in Fig. 18.

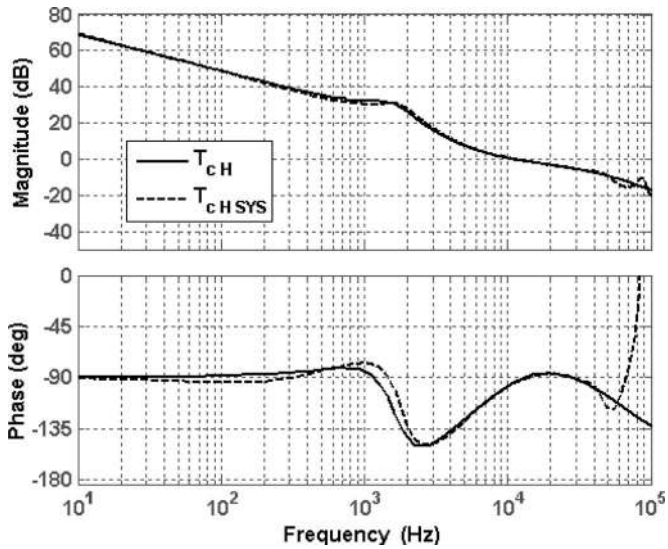

Fig. 21. Loop transfer function of the fully lit SCPVMs in the constrained MPP of Fig. 18 as (solid line) an isolated system and as (dashed line) part of the system of Fig. 2.

parameters as those ones used to draw the Bode plots of Fig. 11).

Of course, transfer functions $T_{c\,L}(s)$ and $T_{c\,L\,\mathrm{SYS}}(s)$ are not defined in this case because the L shaded SCPVMs operate in open loop. The oscillation of $V_{\mathrm{pan}\,L}$ shown in Fig. 20 is due to the effect of the perturbations of the H fully lit SCPVMs. As an example, the effect of variations of $v_{\mathrm{ref}\,2}$ on $V_{\mathrm{pan}\,H+1}$ can be evaluated by means of transfer function (27), which, in this case, becomes

$$G_{v_{\mathrm{pan}\,H+1}v_{\mathrm{ref}\,2}\mathrm{SYS}}(s) = -\frac{G_{i_{\mathrm{LOAD}}v_{\mathrm{ref}}\mathrm{CL}\,2}(s)G_{v_{\mathrm{pan}}v_{\mathrm{LOAD}}\mathrm{OL}\,H+1}(s)Z_{\mathrm{out\,OL}\,H+1}(s)}{1+\frac{\sum_{i=2}^{H}Z_{\mathrm{out\,CL}\,i}(s)+\sum_{H+1}^{H+L}Z_{\mathrm{out\,OL}\,i}(s)}{Z_{\mathrm{out\,CL}\,2}(s)}} \quad (35)$$

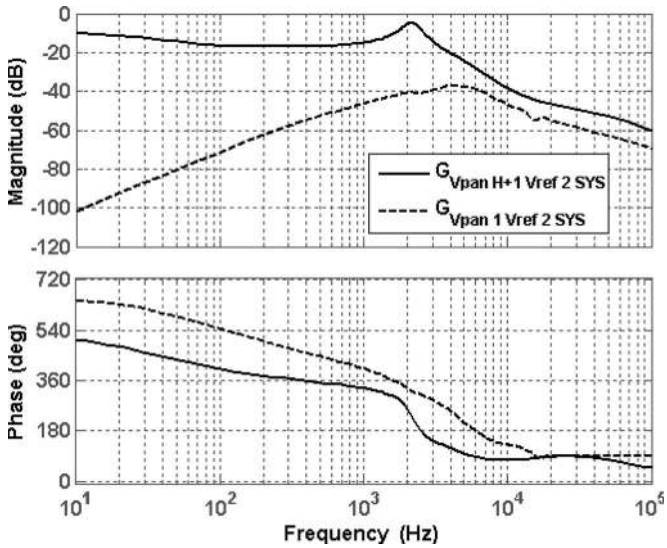

Fig. 22. Bode plots of the transfer functions $G_{v_{\mathrm{pan}\,1}v_{\mathrm{ref}\,2}\mathrm{SYS}}(s)$ and $G_{v_{\mathrm{pan}\,H+1}v_{\mathrm{ref}\,2}\mathrm{SYS}}(s)$.

where subscripts have been used with the same meaning already adopted for (34). Bode plots of the transfer function $G_{v_{\mathrm{pan}H+1}v_{\mathrm{ref}\,2}\mathrm{SYS}}(s)$ are shown in Fig. 22 in the same conditions and for the same values of the parameters used for Fig. 21. In Fig. 22, the Bode plots of the transfer function $G_{v_{\mathrm{pan}\,1}v_{\mathrm{ref}\,2}\mathrm{SYS}}(s)$ are also shown in order to highlight why the variations of $v_{\mathrm{ref}\,2}$ have considerably different effects on $V_{\mathrm{pan}\,1}$ (negligible effects) and on $V_{\mathrm{pan}\,H+1}$ (nonnegligible effects).

The case shown in Fig. 20 is just an example of what can happen. In fact, depending on the operating conditions in terms of irradiation levels, number of SCPVMs in the string, output-voltage levels, etc., it is also possible to obtain situations in which some of the SCPVMs (those ones with the higher irradiation value) operate under duty-cycle limitation (at the upper saturation level D_H) and the remaining SCPVMs operate under duty-cycle limitation (at the lower saturation level D_L). In the general case, by considering the presence of more than two different irradiation levels, it can happen that some SCPVMs operate under duty-cycle limitation at D_H, some other SCPVMs operate under duty-cycle limitation at D_L, and the remaining ones operate under MPPT control. The system under study has been simulated under variable weather conditions by considering a time-varying irradiation on some of the modules [20] and by analyzing the correspondent dynamic properties of the system. It has been verified that the system is stable under such conditions. Results are going to be published in a future work.

VI. Conclusion

The dc and ac analysis of a DMPPT has been presented in this paper. Some useful stability criteria have also been provided. The choices of the dc–dc converter topology and parameters, as well as of the string size and inverter's operating voltage, have been found to be critical steps in the design of a PV system with DMPPT. The optimization of these parameters will be the object of authors' future investigation. Dynamic interaction among SCPVMs has not been found responsible of instability or phase margin degradation for a boost topology. Other topologies such as the SEPIC or isolated converters are currently under study.

References

[1] W. Hoffmann, "PV on the way from a few lead markets to a world market," in *Proc. IEEE WCPEC*, Waikoloa, HI, May 8, 2006, pp. 2454–2456.

[2] J. M. Carrasco, L. G. Franquelo, J. T. Bialasiewicz, E. Galvan, R. C. Portillo Guisado, M. A. M. Prats, J. I. Leon, and N. Moreno-Alfonso, "Power-electronic systems for the grid integration of renewable energy sources: A survey," *IEEE Trans. Ind. Electron.*, vol. 53, no. 4, pp. 1002–1016, Jun. 2006.

[3] S. Liu and R. A. Dougal, "Dynamic multiphysics model for solar array," *IEEE Trans. Energy Convers.*, vol. 17, no. 2, pp. 285–294, Jun. 2002.

[4] G. Petrone, G. Spagnuolo, and M. Vitelli, "Analytical model of mismatched photovoltaic fields by means of Lambert W-function," *Sol. Energy Mater. Sol. Cells*, vol. 91, no. 18, pp. 1652–1657, Nov. 2007.

[5] G. R. Walker and P. C. Sernia, "Cascaded DC–DC converter connection of photovoltaic modules," *IEEE Trans. Power Electron.*, vol. 19, no. 4, pp. 1130–1139, Jul. 2004.

[6] E. Roman, R. Alonso, P. Ibanez, S. Elorduizapatarietxe, and D. Goitia, "Intelligent PV module for grid-connected PV systems," *IEEE Trans. Ind. Electron.*, vol. 53, no. 4, pp. 1066–1073, Aug. 2006.

[7] W. Xiao, N. Ozog, and W. G. Dunford, "Topology study of photovoltaic interface for maximum power point tracking," *IEEE Trans. Ind. Electron.*, vol. 54, no. 3, pp. 1696–1704, Jun. 2007.

[8] N. Femia, M. Fortunato, G. Lisi, G. Petrone, G. Spagnuolo, and M. Vitelli, "Guidelines for the optimization of P&O technique for grid-connected double-stage photovoltaic systems," in *Proc. IEEE Int. Symp. Ind. Electron.*, Vigo, Spain, Jun. 4–7, 2007, pp. 2420–2425.

[9] K. K. Tse, B. M. T. Ho, H. S.-H. Chung, and S. Y. Ron Hui, "A comparative study of maximum-power-point trackers for photovoltaic panels using switching-frequency modulation scheme," *IEEE Trans. Ind. Electron.*, vol. 51, no. 2, pp. 410–418, Apr. 2004.

[10] R. W. Erickson and D. Maksimovic, *Fundamentals of Power Electronics*. Norwell, MA: Kluwer, 2001.

[11] T. Noguchi, S. Togashi, and R. Nakamoto, "Short-current pulse-based maximum-power-point tracking method for multiple photovoltaic-and-converter module system," *IEEE Trans. Ind. Electron.*, vol. 49, no. 1, pp. 217–223, Feb. 2002.

[12] W. Xiao, M. G. J. Lind, W. G. Dunford, and A. Capel, "Real-time identification of optimal operating points in photovoltaic power systems," *IEEE Trans. Ind. Electron.*, vol. 53, no. 4, pp. 1017–1026, Jun. 2006.

[13] I.-S. Kim, M.-B. Kim, and M.-J. Youn, "New maximum power point tracker using sliding-mode observer for estimation of solar array current in the grid-connected photovoltaic system," *IEEE Trans. Ind. Electron.*, vol. 53, no. 4, pp. 1027–1035, Aug. 2006.

[14] J.-M. Kwon, K.-H. Nam, and B.-H. Kwon, "Photovoltaic power conditioning system with line connection," *IEEE Trans. Ind. Electron.*, vol. 53, no. 4, pp. 1048–1054, Jun. 2006.

[15] N. Mutoh, M. Ohno, and T. Inoue, "A method for MPPT control while searching for parameters corresponding to weather conditions for PV generation systems," *IEEE Trans. Ind. Electron.*, vol. 53, no. 4, pp. 1055–1065, Jun. 2006.

[16] N. Mutoh and T. Inoue, "A control method to charge series-connected ultraelectric double-layer capacitors suitable for photovoltaic generation systems combining MPPT control method," *IEEE Trans. Ind. Electron.*, vol. 54, no. 1, pp. 374–383, Feb. 2007.

[17] K. Kobayashi, H. Matsuo, and Y. Sekine, "An excellent operating point tracker of the solar-cell power supply system," *IEEE Trans. Ind. Electron.*, vol. 53, no. 2, pp. 495–499, Apr. 2006.

[18] J.-H. Park, J.-Y. Ahn, B.-H. Cho, and G.-J. Yu, "Dual-module-based maximum power point tracking control of photovoltaic systems," *IEEE Trans. Ind. Electron.*, vol. 53, no. 4, pp. 1036–1047, Jun. 2006.

[19] W. Xiao, W. G. Dunford, P. R. Palmer, and A. Capel, "Regulation of photovoltaic voltage," *IEEE Trans. Ind. Electron.*, vol. 54, no. 3, pp. 1365–1374, Jun. 2007.

[20] N. Femia, G. Petrone, G. Spagnuolo, and M. Vitelli, "Optimization of perturb and observe maximum power point tracking method," *IEEE Trans. Power Electron.*, vol. 20, no. 4, pp. 963–973, Jul. 2005.

[21] C. M. Wildrick, F. C. Lee, B. H. Cho, and B. Choi, "A method of defining the load impedance specification for a stable distributed power system," *IEEE Trans. Power Electron.*, vol. 10, no. 3, pp. 280–285, May 1995.

Nicola Femia (M'94) was born in Salerno, Italy, in 1963. He received the Ph.D. degree (with honors) in engineering of industrial technologies (section of electronics) from the University of Salerno, Salerno, in 1988.

From 1990 to 1998, he was an Assistant Professor, from 1998 to 2001, he was an Associate Professor, and since 2001, he has been a Full Professor of electrotechnics with the Department of Information and Electrical Engineering, University of Salerno. He is the coauthor of about 80 scientific papers published in the proceedings of international symposia and in international journals. His main scientific interests include the fields of circuit theory and applications and power electronics.

Dr. Femia was an Associate Editor for the IEEE TRANSACTIONS ON POWER ELECTRONICS from 1995 to 2003.

Gianpaolo Lisi was born in Salerno, Italy, in 1980. He received the Ph.D. degree in electronic engineering from the University of Salerno, Salerno, in 2008.

He is currently with National Semiconductor Corporation, Santa Clara, CA. His main research interests include the analysis and design of switching converters for renewable energy sources in distributed power systems.

Giovanni Petrone was born in Salerno, Italy, in 1975. He received the "Laurea" degree in electronic engineering from the University of Salerno, Salerno, in 2001, and the Ph.D. in electrical engineering from the University of Naples "Federico II," Naples, Italy, in 2004.

Since January 2005, he has been an Assistant Professor of electrotechnics with the Department of Information and Electrical Engineering, University of Salerno. His main research interests include the analysis and design of switching converters for telecommunication applications, renewable energy sources in distributed power systems, and tolerance analysis of electronic circuits.

Giovanni Spagnuolo (M'98) was born in Salerno, Italy, in 1967. He received the "Laurea" degree in electronic engineering from the University of Salerno, Salerno, in 1993, and the Ph.D. degree in electrical engineering from the University of Naples "Federico II," Naples, Italy, in 1997.

Since 1993, he has been with the Department of Information and Electrical Engineering, University of Salerno, where he was a Postdoctoral Fellow (1998–1999), an Assistant Professor of electrotechnics (1999–2003), and has been an Associate Professor since January 2004. His main research interests include the analysis and simulation of switching converters, circuits and systems for renewable energy sources, and tolerance analysis and design of electronic circuits.

Dr. Spagnuolo is an Associate Editor for the IEEE TRANSACTIONS ON INDUSTRIAL ELECTRONICS.

Massimo Vitelli was born in Caserta, Italy, in 1967. He received the "Laurea" degree (with honors) in electrical engineering from the University of Naples "Federico II," Naples, Italy, in 1992.

In 1994, he was with the Department of Information Engineering, Second University of Naples, Aversa, Italy, as a Researcher, where he was an Associate Professor in 2001, and has been a Full Professor with the Department of Information Engineering, since 2007, teaching courses on electrotechnics. His main research interests include the electromagnetic characterization of new insulating and semiconducting materials for electrical applications, electromagnetic compatibility, and the analysis and simulation of power electronic circuits.

Prof. Vitelli is an Associate Editor for the IEEE TRANSACTIONS ON POWER ELECTRONICS.